THE ASTROPHYSICAL JOURNAL, 527:498–512, 1999 December 20

A DETERMINATION OF H_0 WITH THE CLASS GRAVITATIONAL LENS B1608+656. I. TIME DELAY MEASUREMENTS WITH THE VLA[1]

C. D. FASSNACHT,[2,3] T. J. PEARSON,[2] A. C. S. READHEAD,[2] I. W. A. BROWNE,[4] L. V. E. KOOPMANS,[5] S. T. MYERS,[6] AND P. N. WILKINSON[4]

Received 1999 April 8; accepted 1999 August 2

ABSTRACT

We present the results of a program to monitor the four-image gravitational lens B1608+656 with the VLA. The system was observed over a 7 month period from 1996 October to 1997 May. The 64 epochs of observation have an average spacing of 3.6 days. The light curves of the four images of the background source show that the flux density of the background source has varied at the ~5% level. We measure time delays in the system based on common features that are seen in all four light curves. The three independent time delays in the system are found to be $\Delta t_{BA} = 31 \pm 7$ days, $\Delta t_{BC} = 36 \pm 7$ days, and $\Delta t_{BD} = 76^{+9}_{-10}$ days at 95% confidence. The uncertainties on the time delays are determined by Monte Carlo simulations that use fake light curves that have the characteristics of the observed light curves. This is the first gravitational lens system for which three independent time delays have been measured. A companion paper presents a mass model for the lensing galaxy that correctly reproduces the observed image positions, flux density ratios, and time delay ratios. The last condition is crucial for determining H_0 with a four-image lens. We combine the time delays with the model to obtain a value for the Hubble constant of $H_0 = 59^{+8}_{-7}$ km s^{-1} Mpc^{-1} at 95% confidence (statistical) for $(\Omega_M, \Omega_\Lambda) = (1,0)$. In addition, there is an estimated systematic uncertainty of ± 15 km s^{-1} Mpc^{-1} from uncertainties in modeling the radial mass profiles of the lensing galaxies. The value of H_0 presented in this paper is comparable to recent measurements of H_0 from the gravitational lenses 0957+561, PG 1115+080, B0218+357, and PKS 1830−211.

Subject headings: distance scale — galaxies: individual (B1608+656) — gravitational lensing — radio continuum: galaxies

1. INTRODUCTION

Even before the discovery of the first gravitational lens system, a technique for using gravitational lenses to measure the distance scale of the universe had been developed (Refsdal 1964). The technique requires a lens system in which multiple images of the background source are formed. A "map" of the geodesics along which the light travels to form the images is constructed and used to predict the differences in light travel times along the geodesics. If the background source is variable, these time delays can be measured as each image varies in turn. The ratios between the observed and predicted delays give the Hubble constant in the assumed world model $(\Omega_M, \Omega_\Lambda)$. The use of gravitational lenses for determining H_0 has major advantages over traditional "distance ladder" approaches. First, the technique gives a direct estimate of H_0 at cosmological distances, where the effects of peculiar velocities are minimal. Second, this measurement of H_0 is obtained in one step, without the propagation of errors inherent in the distance ladder approach.

With the discovery that the "double quasar" 0957+561 A,B was a lens system (Walsh et al. 1979), the effort to use lenses to measure H_0 began in earnest. For many years the effort was hindered by both the paucity of known lens systems and the difficulty in measuring time delays in the systems. In fact, an unambiguous time delay has only recently been measured in 0957+561 in spite of over 10 years of intensive monitoring (Kundić et al. 1995, 1997; Oscoz et al. 1997; Haarsma et al. 1999). Another of the earliest known lenses, PG 1115+080 (Weymann et al. 1980), has also just produced measurable time delays (Schechter et al. 1997). However, we may have entered a new era for time delay measurements from gravitational lenses. One reason for this is the accelerated rate of discovery of new lenses from systematic radio surveys. The Jodrell-VLA Astrometric Survey (JVAS; Patnaik et al. 1992; Browne et al. 1998; Wilkinson et al. 1998) has produced six new lenses, and time delays have been measured for one of them (B0218+357; Biggs et al. 1999). The ongoing Cosmic Lens All-Sky Survey (CLASS; S. T. Myers et al. 1999, in preparation) has found 12 new lenses since it began in 1994. This paper reports the first measurement of time delays from a CLASS lens.

The CLASS project is a large search for gravitational lenses with the VLA, with an explicit goal of finding lens systems that can be used to measure H_0. The gravitational lens B1608+656 (R.A. $16^h09^m13^s.956$, decl. $+65°32'28''.971$ [J2000]) was observed in the first phase of CLASS and was immediately recognized as a lens system. The radio discovery image shows four unresolved components in a typical lens geometry (Myers et al. 1995; see Fig. 1 for a

[1] The National Radio Astronomy Observatory is operated by Associated Universities, Inc., under cooperative agreement with the National Science Foundation.

[2] Owens Valley Radio Observatory, California Institute of Technology, 105-24, Pasadena, CA 91125; cdf@astro.caltech.edu, tjp@astro.caltech.edu, acr@astro.caltech.edu.

[3] Present Address: NRAO, P.O. Box O, Socorro, NM 87801; cfassnac@aoc.nrao.edu.

[4] Nuffield Radio Astronomy Laboratories, Jodrell Bank, University of Manchester, Macclesfield, Cheshire SK11 9DL, UK; iwb@jb.man.ac.uk, pnw@jb.man.ac.uk.

[5] Kapteyn Astronomical Institute, Postbus 800, 9700 AV Groningen, Netherlands; leon@astro.rug.nl.

[6] Alfred P. Sloan Fellow, Department of Physics and Astronomy, University of Pennsylvania, 209 South 33rd Street, Philadelphia, PA 19104-6396; myers@upenn5.hep.upenn.edu.

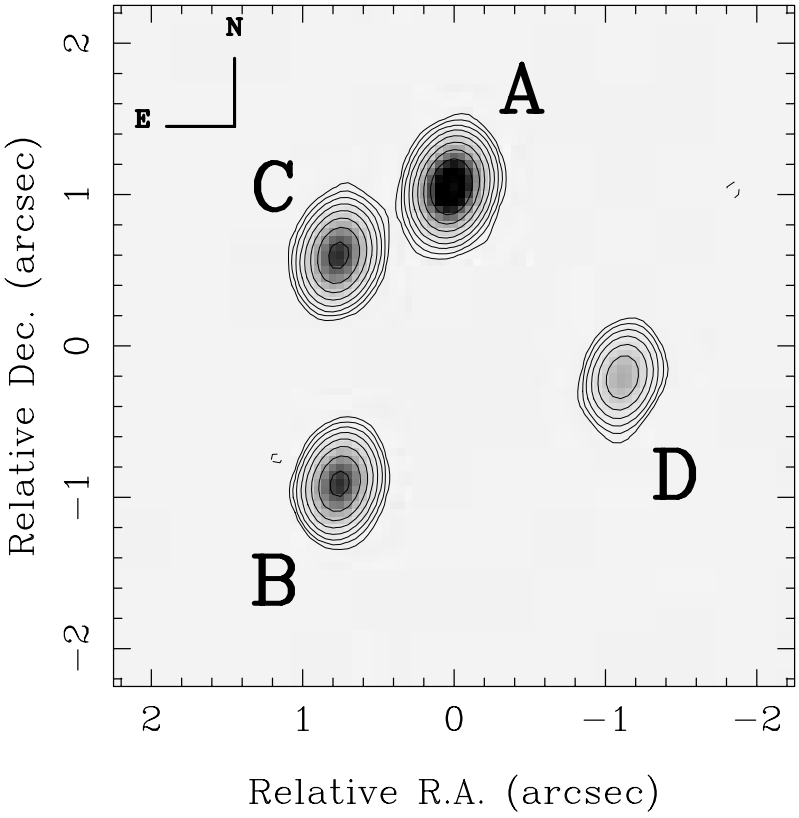

FIG. 1.—Map of B1608+656 from observation on 1996 November 18. The contours are −3, 3, 6, 12, 24, 48, 96, 192, 384, and 768 times the rms noise level of 0.035 mJy beam^{-1}. The map is made by fitting point source components to the (u, v) data and restoring with a 0.″33 × 0.″23 restoring beam.

map of the system). The system was also discovered in a search for gigahertz-peaked spectrum sources and was found to be the lensed core of a classical radio double source (Snellen et al. 1995). Further investigations of the system have provided data crucial for using the system for measuring H_0. We have measured the lens redshift (z_ℓ = 0.630; Myers et al. 1995) and source redshift (z_s = 1.394; Fassnacht et al. 1996). Optical and infrared observations taken with the *Hubble Space Telescope* reveal that the background source is being lensed by a pair of possibly merging galaxies (Jackson, Nair, & Browne 1997). The positions of the lensing galaxies relative to the lensed images are important constraints on models of the lensing potential (Koopmans & Fassnacht 1999, hereafter Paper II). The *Hubble Space Telescope* (*HST*) images also show arcs due to the lensing of stellar emission from the background source. These arcs could be used as further constraints of the lens model.

Flat-spectrum cores of radio galaxies such as the lensed object in B1608+656 are often variable. To test for variability in the B1608+656 background source, we made several observations of the system with the VLA, separated by timescales of months. These data showed that the flux density of the background source varied by up to 15%. The variability makes B1608+656 an excellent candidate for a dedicated monitoring program to determine time delays. This paper presents the results of VLA monitoring from October 1996 to May 1997. These observations have resulted in the measurement of the three independent time delays in the B1608+656 system and a subsequent determination of H_0. The Hubble constant is expressed as H_0 = 100 h km s^{-1} Mpc^{-1}. Throughout this paper we assume (Ω_M, Ω_Λ) = (1,0). The effect of varying the cosmological model is treated in Paper II.

2. OBSERVATIONS

We observed B1608+656 between 1996 October 10 and 1997 May 9, during which time the VLA was in the A, BnA, and B configurations. The 64 epochs were separated, on average, by 3.6 days. The observations were carried out at 8.5 GHz, giving angular resolutions ranging from 0.″25 to 0.″7 in the different array configurations. The observations are summarized in Table 1. The typical observation is 60 minutes long and includes scans on B1608+656, a flux calibrator (3C 286 or 3C 48), a phase calibrator (1642+689) chosen from the VLA calibrator list (Perley & Taylor 1999), and two secondary flux calibrators (1634+627 and 1633+741). The secondary flux calibrators are nearby steep-spectrum sources that are not expected to vary over the timescales of the observations. We observe these sources to determine corrections for errors in the absolute flux calibration from epoch to epoch. The basic observing pattern is:

1642+689 (1 minute on source),
1634+627 (1 minute on source),
B1608+656 (4–6 minutes on source), and
1633+741 (2 minutes on source).

A typical 60 minute observation begins with a 9–10 minute scan (including slew time) on the flux calibrator, contains three repetitions of the basic pattern on B1608+656, and ends with scans on 1642+689 (1 minute) and the flux calibrator again (~3 minutes). For the few

TABLE 1

OBSERVATIONS

Epoch	MJD − 50,000	Array Configuration	Start Time (LST)	t_{tot} (minutes)	t_{1608} (minutes)	Comments
1996 Oct 10.....	366	D → A	16:30	60	27	
1996 Oct 12.....	368	D → A	15:30	30	5	
1996 Oct 16.....	372	D → A	21:00	60	21	
1996 Oct 18.....	374	A	17:30	60	21	
1996 Oct 20.....	376	A	01:30	60	21	Elevation $\leq 30°$. Thunderstorms
1996 Oct 23.....	379	A	17:30	30	6	
1996 Oct 26.....	382	A	14:30	60	18	$T_{sys} > 100$ K .
1996 Oct 29.....	385	A	22:30	30	5	Elevation $\leq 30°$. Gusting winds
1996 Oct 31.....	387	A	20:00	60	18	
1996 Nov 01.....	388	A	18:30	60	18	
1996 Nov 03.....	390	A	18:00	60	21	Wind ≥ 10 m s^{-1}
1996 Nov 07.....	394	A	07:00	30	6	Elevation $\leq 30°$
1996 Nov 08.....	395	A	13:00	60	21	
1996 Nov 11.....	398	A	13:00	60	18	
1996 Nov 12.....	399	A	07:30	30	8	Elevation $\leq 30°$
1996 Nov 15.....	402	A	17:00	60	21	High wind gusts
1996 Nov 18.....	405	A	15:30	60	21	
1996 Nov 23.....	410	A	17:00	60	20	Wind $\geq$ 10 m s^{-1}
1996 Nov 27.....	414	A	21:00	60	20	
1996 Dec 01.....	418	A	14:00	60	20	
1996 Dec 05.....	422	A	14:30	30	7	
1996 Dec 07.....	424	A	15:00	30	5	
1996 Dec 10.....	427	A	17:00	60	20	Wind $\geq$ 10 m s^{-1}
1996 Dec 15.....	432	A	17:00	90	34	
1996 Dec 20.....	437	A	19:15	30	5	
1996 Dec 23.....	440	A	17:30	90	34	
1996 Dec 24.....	441	A	15:30	30	10	
1996 Dec 29.....	446	A	15:00	60	20	
1997 Jan 03.....	451	A	16:30	60	20	Wind ≥ 10 m s^{-1}
1997 Jan 07.....	455	A	18:30	90	35	
1997 Jan 11.....	459	A	16:00	60	20	
1997 Jan 16.....	464	A → BnA	16:00	60	20	
1997 Jan 17.....	465	A → BnA	09:30	30	8	Elevation $\leq 30°$. Flurries
1997 Jan 20.....	468	A → BnA	15:30	60	20	
1997 Jan 26.....	474	BnA	14:00	60	20	Rain
1997 Jan 30.....	478	BnA	13:00	60	19	
1997 Feb 02.....	481	BnA	20:00	60	20	
1997 Feb 08.....	487	BnA	19:00	60	19	
1997 Feb 13.....	492	BnA → B	15:30	60	18	
1997 Feb 18.....	497	B	18:00	60	19	
1997 Feb 23.....	502	B	18:00	60	19	
1997 Feb 28.....	507	B	18:00	60	19	Snow storms.
1997 Mar 03.....	510	B	18:00	60	19	
1997 Mar 08.....	515	B	16:00	60	18	
1997 Mar 14.....	521	B	18:15	75	30	
1997 Mar 16.....	523	B	17:45	45	12	
1997 Mar 21.....	528	B	18:00	60	20	
1997 Mar 25.....	532	B	21:30	60	19	Wind $\geq$ 10 m s^{-1}. Snowing.
1997 Mar 30.....	537	B	19:00	90	30	
1997 Apr 01.....	539	B	17:30	60	20	
1997 Apr 05.....	543	B	18:00	60	20	
1997 Apr 07.....	545	B	18:00	60	20	
1997 Apr 11.....	549	B	18:00	60	20	
1997 Apr 15.....	553	B	18:00	60	20	
1997 Apr 19.....	557	B	15:00	60	18	
1997 Apr 22.....	560	B	18:00	60	20	
1997 Apr 26.....	564	B	18:00	60	20	
1997 May 03.....	571	B	18:00	60	20	
1997 May 08.....	576	B	18:00	90	30	
1997 May 13.....	581	B	18:00	60	20	
1997 May 17.....	585	B	16:30	60	19	
1997 May 21.....	589	B	18:00	60	20	
1997 May 23.....	591	B	18:00	60	20	
1997 May 26.....	594	B	20:00	60	19	

observations that are 30 or 90 minutes in length, the number of repetitions of the basic pattern is altered.

3. DATA REDUCTION

3.1. *Calibration*

The data reduction is separated into two major steps, calibration and mapping. The data for each epoch are calibrated using standard routines in the NRAO data reduction package AIPS. Before calibration, the data quality for all sources is assessed and bad points are flagged with the EDITA and TVFLG tasks. Both of the flux calibrators are heavily resolved by the VLA in A configuration at 8.5 GHz. Hence, we cannot treat the calibrators as point sources without limiting the number of baselines that can be used to calculate phase and gain solutions. In order to increase the number of baselines available for the calculations, we create models of 3C 286 and 3C 48 that incorporate the extended emission from the sources. We combine observations from several epochs with the DBCON task in AIPS. The resulting data sets have excellent (u, v) plane coverage, from which we can make high dynamic-range maps. The mapping, which is performed in the DIFMAP package (Shepherd 1997), consists of alternating iterations of CLEANing (Högbom 1974) and self-calibration. The final lists of CLEAN components are read back into AIPS and serve as the calibrator models.

The procedures for the phase calibrator are simpler because the emission from 1642+689 is dominated by an unresolved component. Thus, the assumption that 1642+689 is a point source leads to adequate phase and gain solutions. These calibration solutions are applied to the B1608+656, 1633+741, and 1634+627 data.

3.2. *Source Maps*

We map the data and determine flux densities using the DIFMAP package. We do not expect to see any structural changes over the course of the observations; only changes in flux densities should be observed. To treat the data from each epoch in a uniform fashion and to shorten the mapping procedure, we create models of the observed source structures from high dynamic-range maps. For epochs with noisy data, these models are needed to fix the locations of the regions of low surface brightness emission, which otherwise would not be well constrained by the data.

To make the high dynamic-range maps of each source, we combine 13 high-quality data sets from A and B configuration observations with the DBCON task. The combined data sets, which have excellent (u, v) coverage, are then mapped in DIFMAP. All the maps are made with natural weighting. The secondary flux calibrators, which have significant emission from extended structures, are mapped by using an iterative cycle of CLEANing and self-calibration. Both phase and amplitude self-calibration are used. The models for these sources consist of the final lists of CLEAN components. The emission from B1608+656 is dominated by the four unresolved images of the background source (Fig. 1). Hence, instead of CLEANing the data, we assign point-source model components to the four images of the background source. We then use the DIFMAP MODELFIT function, which varies the component positions and flux densities to obtain the best fit to the (u, v) plane visibilities. The model-fitting iterations are alternated with phase and amplitude self-calibration. In later rounds of the model fitting, several nearby weak sources are seen in the residual maps. These sources are included in the model for the last few iterations of the model fitting. The nearby sources can be seen in Figure 2; their locations and flux densities are listed in Table 2.

The first step in the mapping procedure at each epoch is to read in the data and perform a phase-only self-calibration against the model of the source. This procedure aligns the phase center of the observation with that of the model and eliminates the need for many early steps of cleaning and self-calibration. After this point, the procedures used for B1608+656 differ from those used for the secondary flux calibrators, as discussed below.

3.2.1. *B1608+656*

For each epoch, we determine the flux densities of the four lensed images in the B1608+656 system as follows. After the initial phase self-calibration step, the model described in the previous section is varied to find the best fit to the (u, v) plane visibilities for that epoch. The component positions are held fixed, and only the flux densities are allowed to vary. After several iterations of model fitting, another phase self-calibration is performed against the new model and more iterations of the model fitting are performed. At this point, the component flux densities and the rms noise in the residual map are recorded in a log file (the PHASECAL data set). We then perform an overall gain calibration on the data, getting one gain correction per antenna for the observation. Typical gain corrections are on the order of 1%–2%. Another round of model fitting is performed, and the final component flux densities and rms noise in the residual map are recorded in the log file (the GSCALE data set). We record the two separate data sets in case the gain calibration introduces any errors that may bias the subsequent analysis. All subsequent analysis is performed on both data sets, and no significant differences are seen in the results.

3.2.2. *Secondary Flux Calibrators*

The steep-spectrum secondary flux-density calibrators contain significant extended emission and should not vary over the course of the observations. We expect that any observed variations in flux density are due to errors in the absolute flux calibration and as such can be expressed as an

TABLE 2

OBJECT POSITIONS AND FLUX DENSITIES

Object	α[a] (arcsec)	δ[a] (arcsec)	$S_{8.4}$[b] (mJy)
B1608+656 A	+0.018	+1.001	34.3
B1608+656 B	+0.757	−0.961	16.8
B1608+656 C	+0.763	+0.548	17.4
B1608+656 D.....	−1.111	−0.256	5.9
B1608+656 N.....	+15.0	+23.6	0.6
B1608+656 S	−13.9	−13.0	0.5
Source 1	−34.7	+167.0	3.4
Source 2	−42.0	−61.2	0.8
Source 3	−178.0	−43.5	0.2
Source 4	−26.7	+24.6	0.2

[a] Positions relative to map center at R.A. $16^h09^m13^s.9530$, decl. $+65°32'27''.998$ (J2000).

[b] Flux densities for B1608+656 components A–D are the mean flux densities over the period of VLA monitoring (see § 3.4).

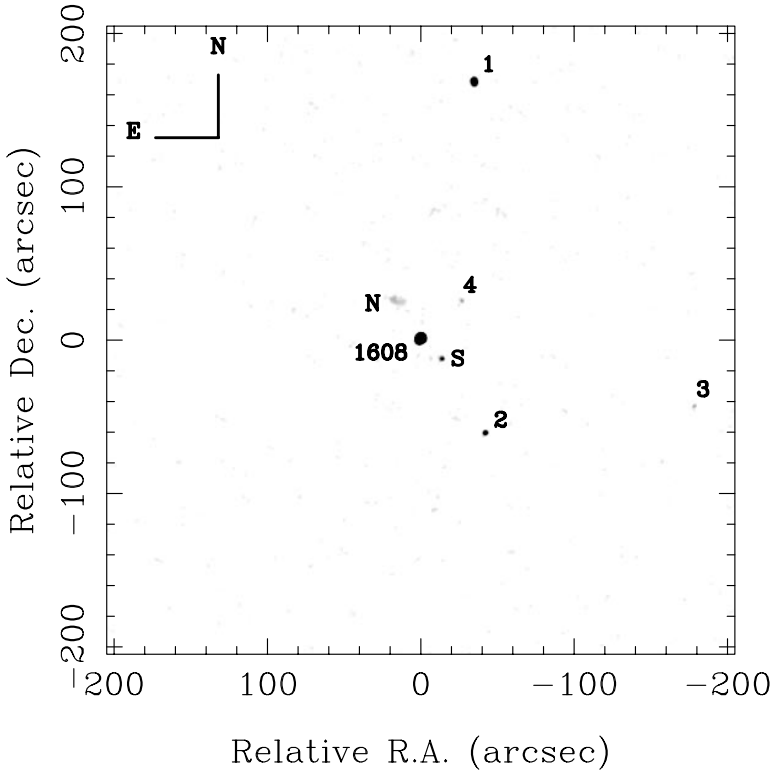

FIG. 2.—Field of B1608+656, showing the lens system and nearby radio sources. The object labeled "1608" consists of the four components shown in Fig. 1. Objects "N" and "S" correspond to the northern and southern radio lobes of B1608+656 seen in low-frequency maps (Snellen et al. 1995).

overall scaling of the model CLEAN component flux densities. That is, the CLEAN component flux densities should not vary with respect to each other. The task of finding the overall flux density of these sources is thus simplified into finding the scale factor μ that, when multiplied by the component flux densities, gives the best fit to the data. To find the best-fit scaling for each data set, we create 11 scaled model files, based on the CLEAN-component models described above. The 11 files have μ ranging from 0.9 to 1.1 in steps of 0.02. Each of the scaled models is compared to the (u, v) plane visibilities, and a reduced χ^2 goodness-of-fit value is returned. We then fit a parabola to the points in the reduced χ^2 curve and find the value of μ that corresponds to the minimum reduced χ^2. This scaling gives the total flux density of the source at that epoch.

3.3. *Light Curve Editing*

Moore & Hewitt (1997), in their analysis of the 15 GHz light curves of the gravitational lens MG 0414+0534, developed objective criteria to flag questionable data. They deleted from their light curves all points associated with observations with the following conditions: the telescope elevations were less than 30°, the wind speed was greater than 10 m s^{-1}, or there was precipitation. We have noted all epochs satisfying their criteria in the "comments" column of Table 1. However, we are able to include many of these points in our analysis because observations at 8.5 GHz are less sensitive to observing conditions than are observations taken at 15 GHz. Therefore, we have excluded only epochs for which the data are severely affected by the observing conditions. This assessment is made by examining the light curves of the secondary calibrator sources. All epochs for which the flux densities of the calibrators deviate by more than 15% from the mean value are deleted. Only two days are deleted after the application of this criterion: 376 and 382 (MJD − 50,000). Note that epoch 376 satisfies two of the flagging criteria defined by Moore & Hewitt. At epoch 382, the system temperatures for all of the telescopes were in the range 100–200 K, as compared to the 30–50 K system temperatures measured for all other epochs. These high system temperatures may have resulted from the fact the subreflectors of several of the antennas had frozen prior to the observation and had just thawed. The signal-to-noise ratios of the maps for epoch 382 were so low that no useful information could be extracted from them. The final edited light curves contain 62 epochs, with an average spacing of 3.7 days. Edited versions of the secondary flux calibrator and B1608+656 light curves are shown in Figures 3 and 4.

3.4. *Secondary Flux Calibration and Final Light Curves*

The normalized light curves of the secondary flux calibrators are shown in Figure 3. As expected for nonvariable sources, the light curves are close to constant. The scatter about the mean is small, with the exception of a few outlying points. All of these outlier points are due to bad observing conditions. The five worst points, for example, occur on days 390, 402, 427, 474, and 532, all of which experienced high winds, precipitation, or both (Table 1). Because of these outliers, the formal calculation of σ overestimates the width of the error distribution. Consequently, we have estimated σ using the interquartile range (IQR), which is less affected by the outliers. For a Gaussian distribution, $\sigma = 0.741\mathrm{IQR}$. For the secondary flux calibrators, we obtain $\sigma = 0.7\%$ and $\sigma = 1.1\%$ for 1634+627 and 1633+741, respectively. Gaussian distributions with these values of σ are reasonable fits to the data (see Fig. 3).

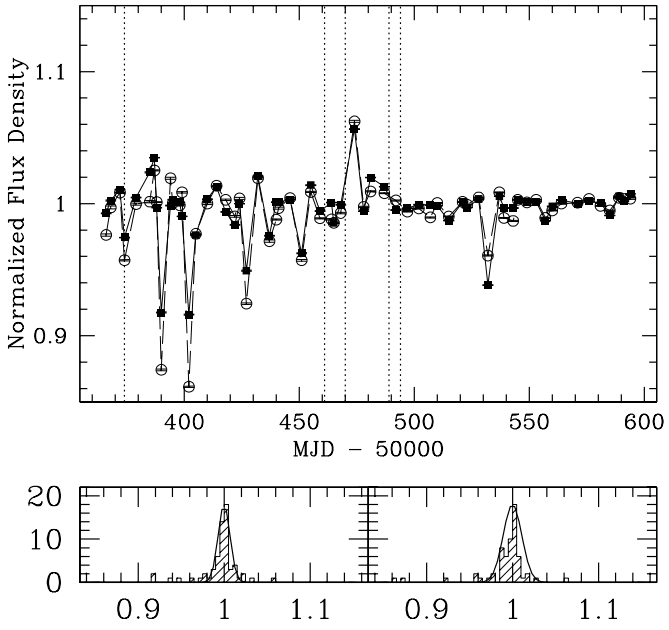

FIG. 3.—*Upper panel:* Light curves of the secondary calibrators 1633+741 (*open circles*) and 1634+627 (*filled squares*). Each curve has been divided by its median value over the length of the observations. The dotted vertical lines represent changes of array configuration. See Table 1 for the array configuration at each epoch. *Lower panels:* Distribution of normalized flux densities about the median values for (*left panel*) 1634+627 and (*right panel*) 1633+741.

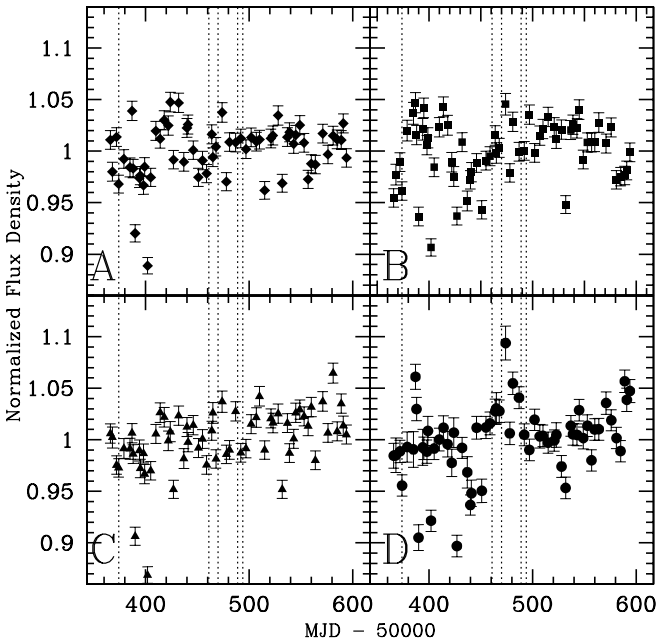

FIG. 4.—Light curves for the four images of the background source in B1608+656 before the secondary flux calibration has been applied. The light curves have been normalized by their mean values such that equal fractional variations in the flux densities of the components will have the same heights in the curves.

The light curves of the two secondary flux calibrators track each other extremely well, suggesting that the observed variations are due to errors in the absolute flux calibration of the data rather than any intrinsic variability of the sources. Because of this, we can use the light curves of the secondary flux calibrators to remove residual flux calibration errors in the B1608+656 component light curves. We create a calibration correction curve by first normalizing the light curves of the secondary flux calibrators and then averaging the two normalized fluxes at each epoch. We then apply the secondary flux calibration by dividing the B1608+656 component light curves by the calibration correction curve. The correction is effective in reducing the scatter in the B1608+656 light curves, as can be seen by comparing Figure 4 to Figure 5. The corrected component light curves are listed in Table 3.[7]

The errors on the final flux densities in Table 3 are a combination of additive and multiplicative terms. The additive uncertainty is well approximated by the rms noise in the residual map at the end of the model fitting. The multiplicative term is indicative of how well the model-fitting procedure is able to find the "true" total flux density of a source. We estimate this error by calculating the ratio of the flux densities of 1634+627 and 1633+741, which we expect not to vary with respect to each other. The flux density ratio is not affected by errors in the absolute flux calibration, so any scatter in the ratio can be attributed to errors in the model-fitting procedure. From the scatter in the flux density ratio, we estimate the fractional error in the component flux densities to be 0.9%; the product of the component flux densities and this value gives the multiplicative uncertainty. The final errors on the flux densities are a combination in quadrature of the additive and multiplicative terms. For the three brightest components (A, B, and C), the multiplicative terms dominate; for component D the multiplicative and additive terms are comparable.

The flux density of a lensed image of the background source is $\mu_i S_\nu$, where S_ν is the true flux density of the background source and μ_i is the magnification associated with the ith (unresolved) image. Similarly, the lensed images will vary by $\mu_i\, dS_\nu$ if the flux density of the background source changes by an amount dS_ν. Hence, any variations in the

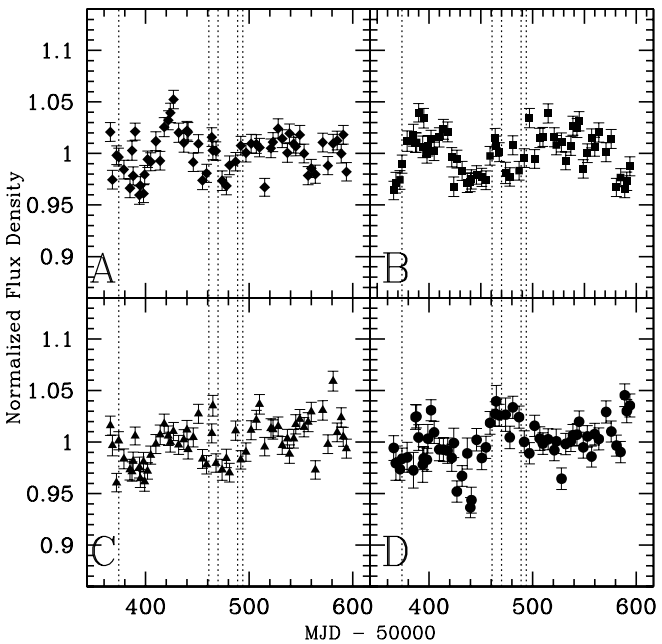

FIG. 5.—Same as Fig. 4 but after the application of the secondary flux calibration.

[7] An electronic version of the light curve table may also be obtained from http://www.nrao.edu/~cfassnac/1608flux.tab.

TABLE 3

FINAL COMPONENT LIGHT CURVES

	FLUX DENSITY (mJy)			
MJD − 50,000	A	B	C	D
366	34.831 ± 0.309	16.106 ± 0.149	17.602 ± 0.162	5.822 ± 0.070
368	33.251 ± 0.307	16.233 ± 0.166	17.269 ± 0.175	5.736 ± 0.097
372	34.063 ± 0.308	16.277 ± 0.151	16.643 ± 0.154	5.701 ± 0.063
374	34.003 ± 0.294	16.532 ± 0.146	17.349 ± 0.153	5.760 ± 0.060
379	33.589 ± 0.307	16.904 ± 0.165	17.042 ± 0.166	5.768 ± 0.085
385	32.972 ± 0.310	17.002 ± 0.176	16.863 ± 0.175	5.695 ± 0.101
387	34.217 ± 0.317	16.883 ± 0.161	16.831 ± 0.160	5.997 ± 0.070
388	33.381 ± 0.299	16.884 ± 0.155	17.002 ± 0.156	6.000 ± 0.066
390	34.845 ± 0.283	17.365 ± 0.149	17.429 ± 0.150	5.881 ± 0.073
394	32.744 ± 0.307	16.811 ± 0.174	16.898 ± 0.175	5.727 ± 0.101
395	33.060 ± 0.297	17.276 ± 0.159	16.715 ± 0.154	5.763 ± 0.064
398	32.795 ± 0.295	16.705 ± 0.154	16.995 ± 0.157	5.755 ± 0.065
399	33.422 ± 0.304	16.830 ± 0.162	16.661 ± 0.161	5.874 ± 0.082
402	33.927 ± 0.271	16.943 ± 0.139	16.840 ± 0.138	6.036 ± 0.060
405	33.846 ± 0.296	16.740 ± 0.150	17.107 ± 0.153	5.910 ± 0.062
410	34.527 ± 0.310	16.966 ± 0.156	17.294 ± 0.159	5.813 ± 0.064
414	33.878 ± 0.308	17.096 ± 0.160	17.447 ± 0.163	5.813 ± 0.067
418	34.996 ± 0.315	17.054 ± 0.159	17.632 ± 0.164	5.807 ± 0.071
422	35.218 ± 0.315	16.645 ± 0.157	17.431 ± 0.164	5.765 ± 0.077
424	35.464 ± 0.323	16.168 ± 0.158	17.324 ± 0.168	5.850 ± 0.084
427	35.909 ± 0.302	16.613 ± 0.144	17.505 ± 0.151	5.574 ± 0.061
432	34.811 ± 0.317	16.423 ± 0.152	17.280 ± 0.160	5.663 ± 0.059
437	34.475 ± 0.308	16.234 ± 0.158	17.368 ± 0.167	5.791 ± 0.088
440	34.875 ± 0.310	16.236 ± 0.147	17.532 ± 0.158	5.483 ± 0.057
441	34.831 ± 0.315	16.286 ± 0.155	17.203 ± 0.163	5.525 ± 0.074
446	33.832 ± 0.304	16.358 ± 0.151	17.405 ± 0.160	5.868 ± 0.064
451	34.444 ± 0.298	16.320 ± 0.146	17.802 ± 0.158	5.765 ± 0.066
455	33.230 ± 0.301	16.271 ± 0.150	17.042 ± 0.157	5.825 ± 0.062
459	33.463 ± 0.298	16.667 ± 0.152	16.946 ± 0.154	5.964 ± 0.064
464	34.451 ± 0.310	16.851 ± 0.156	17.364 ± 0.160	5.979 ± 0.068
465	34.010 ± 0.309	16.720 ± 0.164	17.825 ± 0.173	6.049 ± 0.090
468	33.989 ± 0.305	16.624 ± 0.152	16.867 ± 0.154	5.970 ± 0.063
474	33.015 ± 0.322	16.290 ± 0.172	16.755 ± 0.176	5.974 ± 0.095
478	32.845 ± 0.295	16.223 ± 0.149	16.945 ± 0.156	5.845 ± 0.064
481	33.523 ± 0.306	16.735 ± 0.155	16.709 ± 0.155	6.015 ± 0.063
487	33.643 ± 0.306	16.325 ± 0.151	17.410 ± 0.161	5.960 ± 0.062
492	34.166 ± 0.308	16.528 ± 0.152	16.923 ± 0.155	5.820 ± 0.062
497	33.754 ± 0.304	17.080 ± 0.156	16.961 ± 0.155	5.725 ± 0.060
502	34.051 ± 0.307	16.427 ± 0.150	17.323 ± 0.158	5.879 ± 0.060
507	34.040 ± 0.308	16.761 ± 0.156	17.495 ± 0.162	5.808 ± 0.067
510	33.924 ± 0.307	16.779 ± 0.154	17.754 ± 0.163	5.779 ± 0.061
515	32.624 ± 0.292	17.156 ± 0.156	17.050 ± 0.155	5.804 ± 0.060
521	33.901 ± 0.307	16.774 ± 0.154	17.356 ± 0.159	5.743 ± 0.060
523	34.102 ± 0.310	16.648 ± 0.157	17.337 ± 0.162	5.792 ± 0.069
528	34.548 ± 0.314	16.691 ± 0.155	17.386 ± 0.161	5.582 ± 0.061
532	34.210 ± 0.295	16.394 ± 0.145	17.069 ± 0.150	5.777 ± 0.061
537	33.749 ± 0.307	16.636 ± 0.153	17.181 ± 0.158	5.792 ± 0.058
539	34.388 ± 0.309	16.958 ± 0.155	16.927 ± 0.155	5.826 ± 0.061
543	34.049 ± 0.306	16.921 ± 0.155	17.185 ± 0.157	5.830 ± 0.062
545	33.959 ± 0.308	17.031 ± 0.156	17.422 ± 0.160	5.903 ± 0.060
549	34.338 ± 0.311	16.267 ± 0.150	17.507 ± 0.161	5.758 ± 0.061
553	33.728 ± 0.306	16.519 ± 0.152	17.374 ± 0.160	5.820 ± 0.061
557	33.004 ± 0.295	16.755 ± 0.152	17.459 ± 0.158	5.707 ± 0.060
560	33.241 ± 0.300	16.622 ± 0.152	17.630 ± 0.161	5.833 ± 0.061
564	33.049 ± 0.300	16.850 ± 0.156	16.666 ± 0.154	5.805 ± 0.062
571	34.091 ± 0.309	16.535 ± 0.152	17.653 ± 0.162	5.957 ± 0.063
576	33.332 ± 0.302	16.748 ± 0.154	17.093 ± 0.157	5.847 ± 0.059
581	34.055 ± 0.308	15.971 ± 0.147	18.138 ± 0.166	5.768 ± 0.060
585	34.151 ± 0.307	16.127 ± 0.148	17.287 ± 0.158	5.732 ± 0.060
589	33.723 ± 0.307	15.952 ± 0.148	17.538 ± 0.162	6.051 ± 0.064
591	34.341 ± 0.312	16.068 ± 0.150	17.214 ± 0.160	5.962 ± 0.066
594	33.130 ± 0.302	16.309 ± 0.152	17.018 ± 0.158	5.993 ± 0.065

B1608+656 component light curves that are due to variations in the background source must have the same fractional amplitudes in all four curves. For this reason, the component light curves presented in Figures 4 and 5 are divided by their mean flux densities to allow direct comparison of the fractional variations in the curves. The mean values used to normalize the light curves are 34.29, 16.79, 17.41, and 5.884 mJy for components A, B, C, and D, respectively. All four light curves show variations in flux density at the $\sim 5\%$ level, and there are common features that can be seen in each. Each light curve shows a rise of $\sim 5\%$ in flux density, followed by a plateau lasting ~ 20 days and then a drop of $\sim 4\%$.

4. DETERMINATION OF TIME DELAYS

Models of the B1608+656 system predict that, if the background source is variable, the lensed images will vary in the order B → A → C → D (Myers et al. 1995; Paper II). This is, in fact, the behavior seen in the B1608+656 light curves. In order to determine time delays between component B and the other three components, we have used three statistical methods: (1) smoothing and χ^2 minimization, (2) smoothing and cross-correlation, and (3) dispersion analysis (Pelt et al. 1994, 1996, 1998). The methods are discussed below. All of the analysis has been performed on both the PHASECAL and GSCALE data sets (§ 3.2.1). No significant differences in the results are seen, so we present only the results from the GSCALE set in the subsequent discussion.

4.1. *Methods Using Smoothing/Interpolation*

The first two methods of determining the time delays from the B1608+656 light curves require that the observed data be transferred onto a regular grid. Some previous determinations of time delays (e.g., Kundić et al. 1997; Biggs et al. 1999) have accomplished this transfer by linear interpolation of the data. However, the flux density variations seen in the B1608+656 images are small compared to the noise in the curves; therefore, linear interpolation can amplify noise spikes. In contrast, smoothing reduces the effects of noise compared to the true variations, if the variations have typical timescales significantly longer than the sampling interval. We smooth and resample the data by calculating the weighted mean of points within a smoothing window that is moved from the beginning to the end of the observations in regular steps. The step size is set to 1 day.

We smooth each light curve with several different functions to avoid biasing the results by our choice of weighting function or window size. For completeness, we also include the results obtained from interpolating the data by piecewise linear interpolation. We use the following smoothing schemes: (1) boxcar-weighted mean, (2) triangle-weighted mean, (3) Gaussian-weighted mean, (4) boxcar-weighted mean with a variable-width smoothing window, and (5) triangle-weighted mean with a variable-width window. In the last two schemes, the width of the smoothing window is varied such that the same number of points are always included in the window. We use 3, 5, and 7 point windows for these methods. For the fixed-width window schemes, we smooth with window widths of 5, 10, and 15 days. The Gaussian smoothing scheme uses values of σ equal to 3, 5, and 7 days. In addition to multiplying by the value of the smoothing function, the data points are also variance weighted. Thus, the overall weighting on a point at $t = t_i$ that is being used to calculate a weighted mean at $t = t_k$ is

$$w_i = \frac{(1/\sigma_i^2)g(t_i - t_k)}{\sum_j [(1/\sigma_j^2)g(t_j - t_k)]}, \quad (1)$$

where $g(t)$ is the value of the smoothing function [e.g., $g(t) = 1$ for boxcar smoothing], σ_i is the uncertainty on the flux density at $t = t_i$ (calculated in § 3.4), and the sum is over the points used to calculate the mean. The variance of the weighted mean y at $t = t_k$ in the smoothed curve then becomes

$$\sigma_{y,k}^2 = \frac{1}{\{\sum_i [(1/\sigma_i^2)g(t_i - t_k)]\}^2} \sum_i \frac{[g(t_i - t_k)]^2}{\sigma_i^2}, \quad (2)$$

and $\sigma_{y,k}$ is taken as the uncertainty in the smoothed flux density at that step.

4.1.1. χ^2 *Minimization*

For the χ^2 minimization technique, we compare two light curves, one of which is designated the "control" curve and the other of which is designated the "comparison" curve. Both curves are smoothed, and then the comparison curve is multiplied by a scale factor μ so that its mean flux density is comparable to that of the control curve. After this scaling, the comparison curve is shifted in time by an amount τ with respect to the control curve. We form a grid of (μ, τ) pairs and calculate the χ^2 statistic at each grid point. The step size for τ used in the grid is 1 day and the minimum and maximum shifts are set to ± 114 days, i.e., half of the total length of the observations. The amplitude scale factors are set as percentages of the scale factor μ_0 that equalizes the mean flux densities of the two curves being compared. The scale factors used in the grid range from $0.9\mu_0$ to $1.1\mu_0$, in steps of $0.001\mu_0$.

One result of the smoothing and interpolation performed on the input light curves is that the points in the interpolated curves are no longer independent. When computing the reduced χ^2 statistic we estimate an effective number of independent points, $N_{\rm eff}$, in the overlapping region between the shifted and unshifted curves. This quantity is set to the number of points that would have been present in the overlapping region if the original light curves had been regularly sampled at the average spacing of 3.7 days. This simplifying assumption should not significantly affect the quantity in which we are interested, which is the location of the minimum on the χ^2 surface. In fact, the χ^2 minimization method finds delays that match closely those found from the completely noninterpolative dispersion method (§ 4.2), indicating the robustness of the delays determined from this method.

We repeat the χ^2 minimization three times, once for each independent pair of light curves. The component B light curve is always taken as the control curve. In the three repetitions of the χ^2 minimization, the comparison curves are A, C, and D, respectively. The minimum delay is found by fitting a parabola to the points at the minimum of the gridded χ^2 curve. Tables 4 and 5 summarize the results. Typical goodness-of-fit curves for the three pairs of light curves are shown in Figure 6.

4.1.2. *Cross-Correlation*

For the cross-correlation calculations the component B light curve is once again taken as the control curve. Before the cross-correlations are performed, both the comparison

TABLE 4

TIME DELAYS FROM χ^2 MINIMIZATION AND CROSS-CORRELATION

SMOOTHING FUNCTION	SMOOTHING "WIDTH"[a]	χ^2 MINIMIZATION			CROSS-CORRELATION		
		Δt_{BA}	Δt_{BC}	Δt_{BD}	Δt_{BA}	Δt_{BC}	Δt_{BD}
Boxcar	5	30.97	35.96	74.27	28	36	74
	10	29.25	36.24	75.32	29	37	75
	15	31.84	36.10	75.58	32	36	75
Triangle	5	29.16	36.07	74.20	28	36	74
	10	29.35	35.63	75.27	29	35	75
	15	30.77	36.03	75.97	30	36	76
Gaussian	3	30.65	35.93	75.93	30	36	76
	5	31.55	36.17	76.70	31	37	76
	7	31.52	36.37	77.06	31	37	77
Variable width boxcar	3	30.13	35.79	76.58	30	36	75
	5	29.92	36.18	77.32	30	37	78
	7	29.44	36.38	77.22	30	39	77
Variable width triangle.....	3	30.52	35.84	76.48	30	36	76
	5	30.74	36.22	77.03	30	37	77
	7	29.93	36.25	77.21	30	37	77
Interpolation	...	29.02	36.09	74.82	28	36	74

[a] "Width" is width of window for boxcar and triangle smoothings, σ for Gaussian smoothing, and number of points in window for variable-width smoothings.

and control curves are smoothed and then divided by their mean values over the observations. The normalization by the mean value puts the fractional variations in the light curves at the same level. The cross-correlation functions are computed in the time domain, with the value at each lag calculated in the standard fashion:

$$r_{jk} \equiv \frac{s_{jk}^2}{s_j s_k}, \tag{3}$$

where s_{jk}^2 is the covariance defined by

$$s_{jk}^2 = \frac{[1/(N-1)] \sum_i \{[1/(\sigma_{ij}^2 + \sigma_{ik}^2)](x_{ij} - \bar{x}_j)(x_{ik} - \bar{x}_k)\}}{(1/N) \sum_i [1/(\sigma_{ij}^2 + \sigma_{ik}^2)]} \tag{4}$$

and N is the number of overlapping points (e.g., Bevington 1969). Note that in x_{ij} or σ_{ij}, the first subscript refers to a particular observation and the second subscript to the name of the variable under discussion. Thus x_{ij} is the ith observation of variable x_j. The variance, s_j^2, is given by

$$s_j^2 = \frac{[1/(N-1)] \sum_i [(1/\sigma_i^2)(x_{ij} - \bar{x}_j)^2]}{(1/N) \sum_i (1/\sigma_i^2)}, \tag{5}$$

where the means are weighted means,

$$\bar{x}_j = \frac{\sum_i [(1/\sigma_i^2) x_{ij}]}{\sum_i (1/\sigma_i^2)}. \tag{6}$$

The cross-correlation calculations are repeated for all of the smoothing functions described in § 4.1. In all cases, clear peaks in the cross-correlation curves are seen. Typical curves are shown in Figure 7. The lags at which the peak correlation coefficients occur are given in Table 4. The average displacement between the cross-correlation and χ^2 minimization lags for each pair of curves is less than 1 day.

TABLE 5

FLUX DENSITY RATIOS FROM χ^2 MINIMIZATION

Smoothing Function	Smoothing "Width"	S_A/S_B	S_C/S_B	S_D/S_B
Boxcar	5	2.0387	1.0368	0.3506
	10	2.0383	1.0378	0.3508
	15	2.0411	1.0379	0.3508
Triangle	5	2.0387	1.0368	0.3505
	10	2.0400	1.0376	0.3507
	15	2.0409	1.0379	0.3511
Gaussian	3	2.0407	1.0378	0.3511
	5	2.0411	1.0379	0.3511
	7	2.0410	1.0379	0.3508
Variable width boxcar	3	2.0406	1.0383	0.3511
	5	2.0415	1.0384	0.3512
	7	2.0413	1.0382	0.3512
Variable width triangle.....	3	2.0407	1.0383	0.3511
	5	2.0414	1.0384	0.3512
	7	2.0393	1.0382	0.3512
Interpolation	...	2.0394	1.0374	0.3506

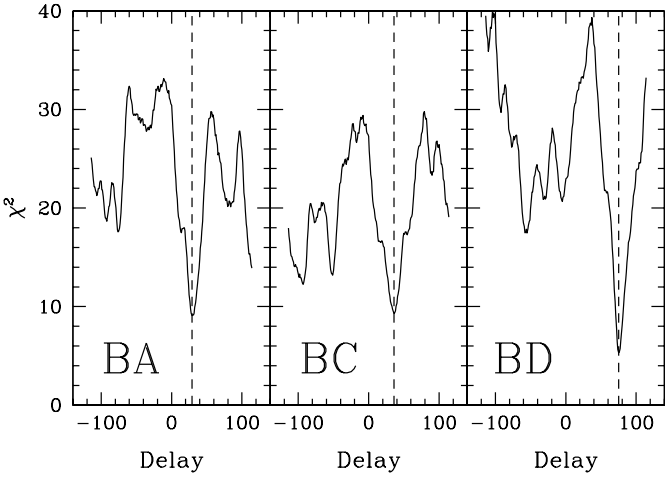

FIG. 6.—Reduced χ^2 vs. lag from comparison of the light curves of components (*left panel*) B and A, (*middle panel*) B and C, and (*right panel*) B and D. Each light curve is smoothed with a boxcar of width 10 days before the χ^2 curves are calculated. The minima (*vertical dashed lines*) are at lags of 29.3, 36.2, and 75.3 days, respectively.

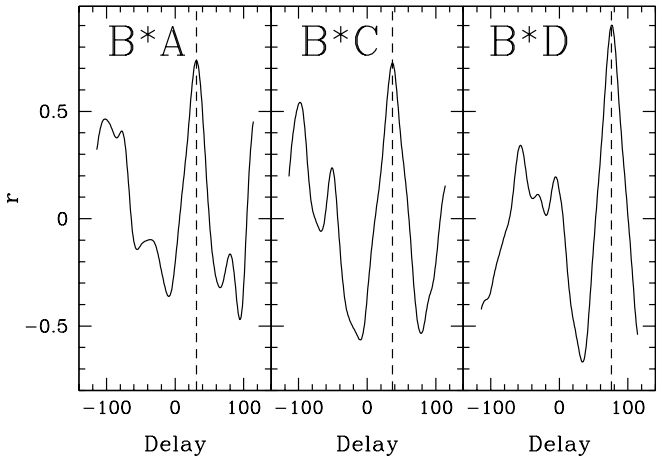

FIG. 7.—Correlation coefficient vs. lag from comparison of the light curves of components (*left panel*) B and A, (*middle panel*) B and C, and (*right panel*) B and D. Each light curve was smoothed with a Gaussian with $\sigma = 5$ days before the cross-correlations were calculated. The maxima (*vertical dashed lines*) are at lags of 31, 37, and 76 days.

4.2. *Dispersion Analysis*

The dispersion analysis methods presented by Pelt et al. (1994, 1996, 1998) do not involve any interpolation of the component light curves. These methods thus have the advantage of avoiding effects introduced by the interpolation and smoothing associated with the methods discussed in § 4.1. The dispersion analysis begins with the construction of a composite curve $C_k(t_k)$ from two input light curves A_i and B_j. Curve A_i is not modified, while curve B_j is scaled by a flux density ratio μ and shifted in time by a delay τ, i.e.,

$$C_k(t_k) = \begin{cases} A_i\,, & \text{if } t_k = t_i\,, \\ \mu B_j\,, & \text{if } t_k = t_j + \tau \end{cases} \qquad (7)$$

(Pelt et al. 1996). We have used a grid of (μ, τ) pairs to construct the C_k curves. Aside from changing the spacing on the delay axis to 0.5 days, the grid limits and spacings are the same as those used in the χ^2 minimization analysis presented in § 4.1.1. The internal dispersion in each curve is calculated, and the grid point associated with the minimum dispersion is recorded. In our analysis of the B1608+656 light curves we calculate dispersions using the nonparametric D_2^2 and the one-parameter $D_{4,2}^2$ statistics, where the notation is taken from Pelt et al. (1996; note that these statistics are called D_1^2 and D_2^2, respectively, in Pelt et al. 1998). The D_2^2 dispersion is calculated using only immediately adjacent points in the composite curve, with the caveat that a pair of points contributes to the dispersion only if the two points are from different input curves. The $D_{4,2}^2$ dispersion is similar but uses all pairs of points that lie within a time range δ of each other. For a detailed description of these estimates, see Pelt et al. (1996). Table 6 gives the results for the D_2^2 analysis and the $D_{4,2}^2$ analysis with several values of the δ parameter. The results do not depend strongly on the value of δ and are consistent within the

TABLE 6

DISPERSION ANALYSIS RESULTS

Statistic	δ	Δt_{BA}	Δt_{BC}	Δt_{BD}	S_A/S_B	S_C/S_B	S_D/S_B
D_2^2	...	30.5	2.0388	36.5	1.0372	74.5	0.3505
$D_{4,2}^2$	3.5	32.0	2.0429	35.5	1.0361	74.5	0.3501
$D_{4,2}^2$	4.5	31.5	2.0429	36.5	1.0372	74.5	0.3502
$D_{4,2}^2$	5.5	31.0	2.0429	37.0	1.0372	76.5	0.3509
$D_{4,2}^2$	6.5	31.0	2.0429	34.5	1.0361	76.5	0.3509
$D_{4,2}^2$	7.5	31.5	2.0429	35.0	1.0372	76.5	0.3509
$D_{4,2}^2$	8.5	32.0	2.0429	35.0	1.0372	77.0	0.3512
$D_{4,2}^2$	9.5	31.5	2.0449	34.5	1.0372	77.5	0.3512
$D_{4,2}^2$	10.5	31.5	2.0449	35.0	1.0372	77.0	0.3512
$D_{4,2}^2$	11.5	32.0	2.0449	35.5	1.0372	77.5	0.3512
$D_{4,2}^2$	12.5	32.0	2.0449	36.5	1.0372	78.5	0.3512
$D_{4,2}^2$	13.5	32.0	2.0449	35.5	1.0372	78.5	0.3512
$D_{4,2}^2$	14.5	32.5	2.0449	35.0	1.0372	78.5	0.3512
$D_{4,2}^2$	15.5	33.0	2.0449	34.5	1.0372	77.5	0.3512
$D_{4,2}^2$	16.5	32.5	2.0449	35.0	1.0372	79.5	0.3516
$D_{4,2}^2$	17.5	32.5	2.0449	35.0	1.0372	79.0	0.3512
$D_{4,2}^2$	18.5	32.0	2.0429	35.0	1.0372	79.5	0.3512
$D_{4,2}^2$	19.5	32.0	2.0429	35.0	1.0372	79.5	0.3512
$D_{4,2}^2$	20.5	32.0	2.0429	35.0	1.0372	80.0	0.3516

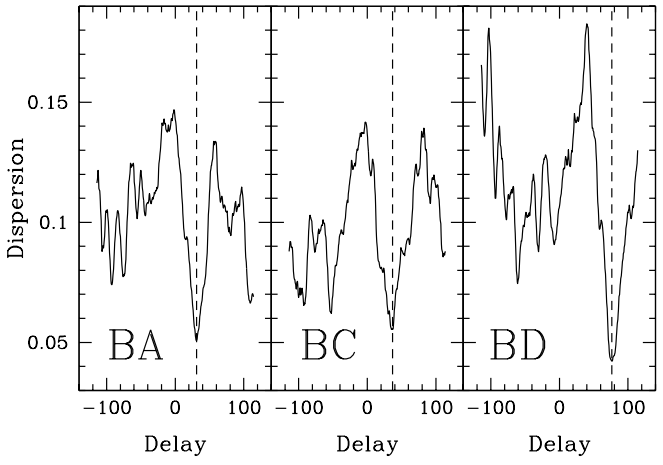

FIG. 8.—Dispersion spectra from comparison of the light curves of components (*left panel*) B and A, (*middle panel*) B and C, and (*right panel*) B and D. The spectra were calculated with the $D^2_{4,2}$ method with $\delta = 5.5$ days. The minima (*vertical dashed lines*) are at lags of 31, 37, and 77 days.

errors (§ 5.2) with the results from the χ^2 minimization and cross-correlation analyses. The dispersion spectra plotted in Figure 8 are cuts through the (μ, τ) grid at a value of μ corresponding to the minimum dispersion.

4.3. *Time Delays*

There is some scatter in the results presented in Tables 4 and 6, which is not surprising considering the low levels of variation and sparse sampling of the light curves. However, the scatter is small compared with both the length of the time delays and the uncertainties in the delays that we find from the Monte Carlo simulations in § 5.2. For each of the three methods used to find the delays (χ^2 minimization, cross-correlation, and dispersion analysis), we take the median values of the delays in Tables 4 and 6. The three median values for each delay are then averaged to obtain $\Delta t_{BA} = 31$ days, $\Delta t_{BC} = 36$ days, and $\Delta t_{BD} = 76$ days. The median flux density ratios, computed in a similar manner, are found to be $S_A/S_B = 2.0418$, $S_C/S_B = 1.0376$, and $S_D/S_B = 0.3512$. We shift the light curves by the mean delays and normalize them using the mean flux density ratios to create a composite light curve of the background source (Fig. 9). A composite curve constructed from the smoothed and interpolated component light curves is shown in Figure 10.

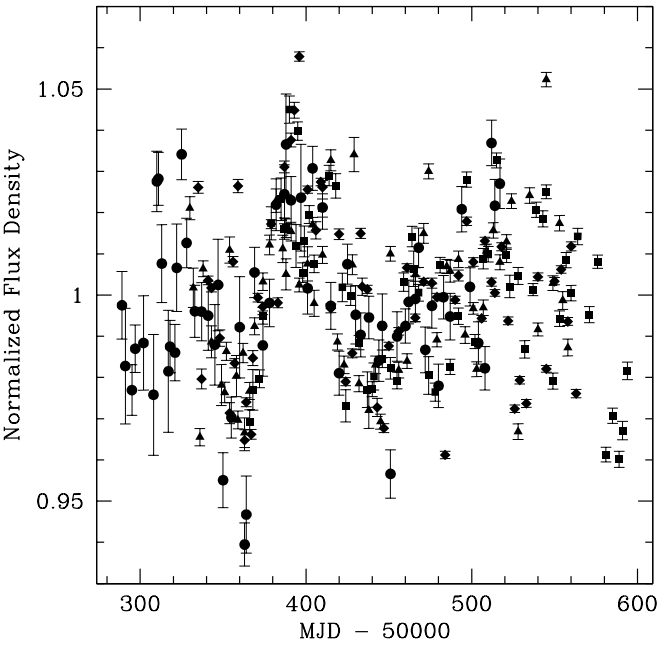

FIG. 9.—Composite light curve constructed by normalizing the component light curves and shifting by the lags given in § 4.3 for components A (*squares*), B (*diamonds*), C (*triangles*), and D (*circles*). For clarity of presentation, error bars represent only the additive component contributed by the rms noise in the maps (see § 3.4).

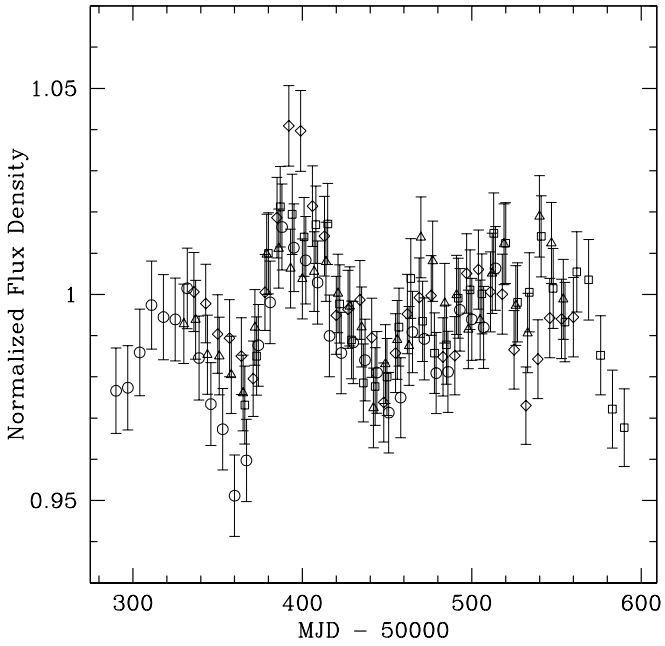

FIG. 10.—Composite light curve constructed as in Fig. 9, but using smoothed rather than raw light curves. The curves are smoothed with a boxcar of width 15 days. For clarity, only one of every seven points is shown for each curve.

5. MONTE CARLO SIMULATIONS

5.1. *Significance of Light Curve Correlations*

The variations seen in the B1608+656 light curves are not large, either in a fractional or absolute sense, compared to what has been seen in other lens systems. The fractional variations seen in B0218+357, 0957+561, and PG 1115+080 are all 2–3 times larger than those seen in B1608+656 (Biggs et al. 1999; Kundić et al. 1995, 1997; Schechter et al. 1997), and PKS 1830−211 shows 50% variations in flux density (although the time delay measurement is based on smaller variations; Lovell et al. 1998). A sceptic might argue that the correlations between the B1608+656 light curves are not significant and could be duplicated by any set of light curves containing random scatter about a constant value.

In theory, the value of the correlation coefficient can be used to assess the significance of the correlation. With the coefficient, r calculated as described in § 4.1.2, the probability of obtaining a value $\geq r$ from two uncorrelated curves of Gaussian-distributed random variables is

$$P_c(r, N) = 2 \int_{|r|}^{1} P_r(\rho, v)\, d\rho \ , \qquad (8)$$

where

$$P_r(r, \nu) = \frac{1}{\sqrt{\pi}} \frac{\Gamma[(\nu+1)/2]}{\Gamma(\nu/2)} (1-r^2)^{(\nu-2)/2} \quad (9)$$

and $\nu = N - 2$ (e.g., Bevington 1969). However, the smoothing and interpolation performed on the sparsely sampled B1608+656 light curves makes the interpretation of the significance of the value of r complicated. The difficulty lies in assessing the number of independent points in the curves at each lag. Monte Carlo simulations show that the number of independent points cannot be estimated simply as the width of the overlap region divided by the width of the smoothing window (i.e., the number of smoothing windows in the overlap region). This calculation underestimates the number of independent points in the region. Because it is difficult to determine the significance of the correlation analytically, we perform Monte Carlo simulations to find the significance empirically. In the simulations, we calculate correlations between light curves consisting of randomly distributed data. To create random light curves with the same distribution of flux densities as seen in the data, we simply randomize the time series for the component light curves while preserving the flux densities at their measured values. By randomizing the times at which the flux densities are measured, we destroy any possible correlations between the curves. Each light curve is randomized independently to avoid correlations at zero lag that are associated with measurement errors.

The simulations are conducted with 3000 sets of randomized curves. Each set of light curves is processed in the manner described in § 4.1.2 and produces three sets of correlation curves (B-A, B-C, and B-D). All values of the correlation coefficient are recorded. The distributions of the cross-correlation values obtained from the 10 day boxcar smoothing scheme are shown in Figure 11. The empirical probabilities of obtaining at least the observed peak values (*vertical dashed lines* in Fig. 11) from uncorrelated curves are all low, with $P(|r| \geq |r_A|) = 2.8 \times 10^{-4}$, $P(|r| \geq |r_C|) = 4.3 \times 10^{-3}$, and $P(|r| \geq |r_D|) < 1.5 \times 10^{-6}$. It is even more unlikely that three pairs of randomized curves could produce three such anomalously high cross-correlation peaks. There can thus be no significant doubt that the correlations we measure are real.

5.2. *Uncertainties in Time Delays and Flux Density Ratios*

The time delay measurement uncertainties contribute directly to the error budget for measuring H_0 with a gravitational lens. In particular, the fractional uncertainties in the time delays contribute a matching fractional uncertainty in H_0, i.e.,

$$\frac{(\sigma_H)_{\rm delay}}{H_0} = \frac{\sigma_{\Delta t}}{\Delta t} . \quad (10)$$

We estimate the uncertainties in the time delays by performing Monte Carlo simulations of the observations. In the simulations we assign time delays between the pairs of light curves and then see how well we can recover the input delays. We also use the simulations to estimate the uncertainties in the flux density ratios, which are necessary for modeling the lensing potential (Paper II).

We produce fake curves with the same characteristics as our real data by smoothing the composite light curve (Fig. 9) with a 10 day boxcar filter. This normalized and smoothed curve is the master light curve for the simulations, representing the assumed true behavior of the background source. The offsets between the points of the composite curve and the master curve are distributed as a zero-mean Gaussian with $\sigma = 0.014$. Note that this is a fractional value since all of the light curves have been normalized to create the master light curve. The Gaussian distribution is used to generate the random offsets for the simulations. The appropriate rescaling of the random offsets is achieved through equation (11). We note that smoothing procedure used in constructing the master curve destroys information on possible short-timescale variations. Thus, if such short-term variations do exist, their effects will be attributed to measurement and calibration errors in this method. However, given the low level of variability of the background source during the observations and the sparse sampling, it is difficult to distinguish any possible short-term variations from measurement error. Thus, we accept $\sigma = 0.014$ as an indication of the measurement error, but with the caveat that the uncertainties in the time delays derived from the Monte Carlo simulations described below may be overestimated.

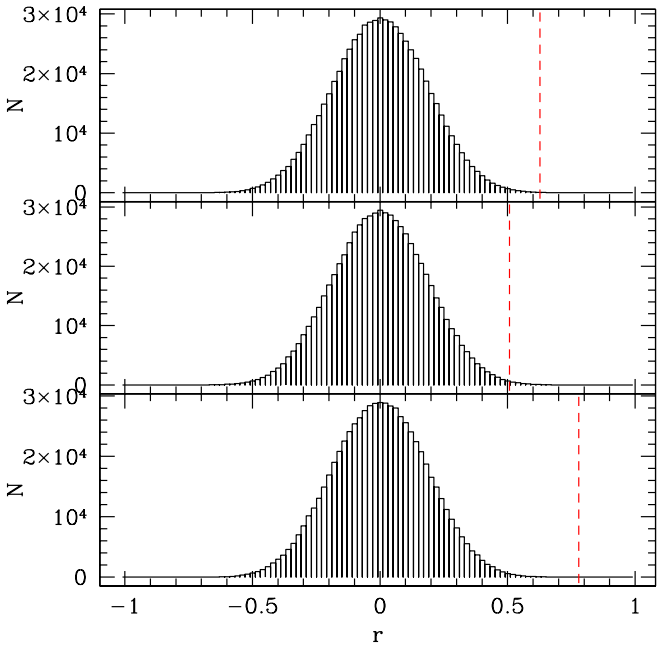

FIG. 11.—Distribution of cross-correlation values obtained from 3000 Monte Carlo simulations of randomized light curves. The distributions presented in this figure are obtained by smoothing the light curves with a boxcar of width 10 days. The dashed vertical lines represent the peak cross-correlation values obtained from the real data.

For each round of the simulation we generate four sparsely sampled fake light curves. The flux density for component j at a time t_i in the fake curves is given by

$$S_j(t_i) = S_B R_j[S_0(t_i + \Delta t_j) + n_{ij}] , \qquad j = \text{A, B, C, D} , \quad (11)$$

where $S_0(t)$ is the normalized master flux density, R_j are the input flux density ratios (2.0418, 1.000, 1.0376, and 0.3512), Δt_j are the input time delays (31, 0, 36, and 76 days), and n_{ij} is the random offset. The four curves are sampled with the pattern used in the observations (see Table 1). The flux density error at each point in the sparsely sampled curves is

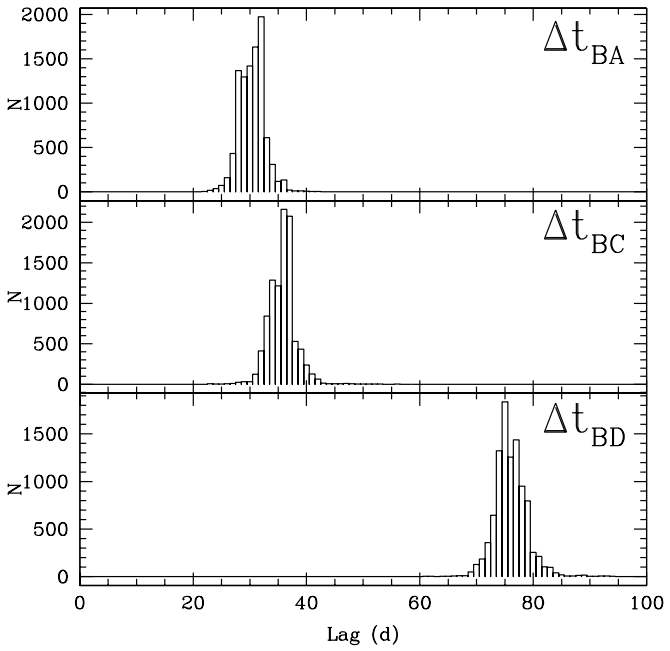

FIG. 12.—Distribution of time delays recovered from cross-correlation analysis of 10,000 Monte Carlo simulations of the B1608 + 656 component light curves. The distributions provide estimates of the uncertainties in the time delays.

set to the observed flux density error for that epoch (see § 3.4).

The fake curves are processed in the manner described in § 4. The best-fit time delays and flux density ratios for each simulation are recorded. Histograms of typical distributions of time delays from 10,000 repetitions of the above procedure are shown in Figure 12. The distributions are non-Gaussian, both in the shape of the peak of the distribution and in the long tail of outliers at negative delays. Thus, we determine the confidence limits by finding the range of delays inside which 95% of the simulation results lie, rather than fitting a Gaussian to the distribution. The limits are chosen such that the minimum range of delays that encloses both the median value and 95% of the simulation results is found. The results for the χ^2 minimization and cross-correlation techniques are given in Table 7. We conservatively take the broader distribution in each case as our estimate of the 95% confidence contours. Thus, we estimate the time delays to be $\Delta t_{BA} = 31 \pm 7$ days, $\Delta t_{BC} = 36 \pm 7$ days, and $\Delta t_{BD} = 76^{+9}_{-10}$ days at 95% confidence.

We have also run Monte Carlo simulations in which the sampling pattern is varied, following the method used in Biggs et al. (1999). The distributions of time delays do not differ significantly from those presented above.

6. DISCUSSION

The goal of monitoring a gravitational lens system is to measure time delays that can then be combined with a model of the lensing potential to produce a measurement of H_0. We have been successful in measuring the three independent time delays in the B1608 + 656 system. Paper II presents a model for the B1608 + 656 system. The model is based on the time delays and flux density ratios presented here, and on positions from VLBA (C. D. Fassnacht et al. 1999, in preparation) and *HST* observations of the system (Jackson et al. 1997). The lensing potential contains contributions from the two lensing objects seen in *HST* images of the system (Jackson et al. 1997), each of which is modeled as an elliptical isothermal mass distribution. The effects of varying the positions of the lensing galaxies, of changing the nature of the lensing galaxy cores (singular or nonsingular), and of departing from an isothermal profile are all explored. The best-fit model is obtained through a simulated annealing process. It correctly reproduces the positions and flux density ratios of the lensed images (with the exception of the D/A flux density ratio). Most importantly, the predicted time delay ratios match the observed time delay ratios to within 1%. Although the individual time delays depend on the Hubble constant ($\Delta t_i \propto h^{-1}$), the time delay ratios have no H_0 dependence. Thus, the model for any lens system with more than two images must correctly reproduce the observed time delay ratios if it is to be used in the determination of H_0. In this sense, gravitational lenses that produce more than two images can put stronger constraints on lens models than can two image lenses, as long as the time delays can be measured.

The B1608 + 656 system is the first four-image lens for which the three independent time delays have been measured and for which a model correctly reproduces the time delay ratios. The best-fit isothermal model from Paper II predicts time delays of $\Delta t_{BA} = 18.0\ h^{-1}$ days, $\Delta t_{BC} = 21.4\ h^{-1}$ days, and $\Delta t_{BD} = 44.9\ h^{-1}$ days. Combining these predicted values with the observed time delays gives three individual determinations of H_0: $(H_0)_{BA} = 58.1$, $(H_0)_{BC} = 59.4$,

TABLE 7

MONTE CARLO SIMULATION RESULTS

			CONFIDENCE INTERVALS		
QUANTITY	INPUT VALUE	METHOD[a]	68%	90%	95%
Δt_{BA}	31	1	28.6–33.0	26.7–34.9	24.4–37.3
Δt_{BC}	36	1	33.5–38.7	31.8–40.3	29.0–43.3
Δt_{BD}	76	1	73.2–78.9	71.1–81.0	67.4–84.7
Δt_{BA}	31	2	29–34	27–36	25–38
Δt_{BC}	36	2	33–38	31–40	29–42
Δt_{BD}	76	2	71–77	68–80	66–82
S_A/S_B	2.0418	1	2.0386–2.0506	2.0344–2.0549	2.0322–2.0570
S_C/S_B	1.0376	1	1.0340–1.0401	1.0318–1.0422	1.0306–1.0433
S_D/S_B	0.3512	1	0.3500–0.3525	0.3492–0.3534	0.3487–0.3539

[a] Method used to calculate delays or flux density ratios: 1 = χ^2 minimization; 2 = cross-correlation.

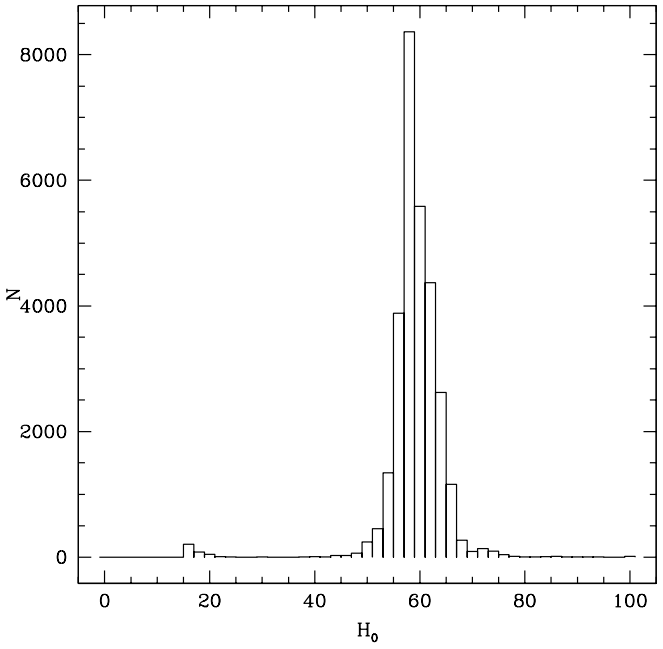

FIG. 13.—Distribution of estimates of H_0 from Monte Carlo simulations. This distribution is formed by converting the time delay simulation results into three H_0 distributions and then combining the individual distributions.

and $(H_0)_{BD} = 59.1$ km s^{-1} Mpc^{-1}. We combine these by calculating a weighted mean of $(H_0)_{1608} = 59.0$ km s^{-1} Mpc^{-1}, where the weights are derived from the uncertainties in the time delays from § 5.2. Note that the B-D value dominates the mean since it has the smallest fractional uncertainty. In order to estimate the uncertainty on $(H_0)_{1608}$, we use the results of the Monte Carlo simulation presented in § 5.2. The distribution of time delays from the simulations are converted into distributions of H_0 by dividing the predicted delays from the Paper II model by the simulation results. The resulting H_0 distributions from the B-A, B-C, and B-D delays are combined into an overall distribution, which is shown in Figure 13. The confidence limits are estimated by finding the ranges that enclose 68%, 90%, and 95% of the data. The resulting 95% confidence limits are $(H_0)_{1608} = 59^{+8}_{-7}$ km s^{-1} Mpc^{-1}. These confidence limits are very close to the statistical 95% limits derived from the lens model, which includes H_0 as a model parameter (59^{+7}_{-6} km s^{-1} Mpc^{-1}; Paper II).

The above estimates of the uncertainties in the determination of H_0 have not included the systematic effects from the choice of the radial mass profile in the lens modeling. The estimated systematic error is ± 15 km s^{-1} Mpc^{-1} (Paper II). It may be possible to reduce this error by modeling the extended lensed stellar emission from the background source, as has been done with the radio Einstein ring MG 1654+1346 (Kochanek 1995). This modeling approach is being conducted by G. Surpi & R. Blandford (1999, private communication).

7. SUMMARY

We have presented the results of an intensive program of monitoring the four-image lens system B1608+656 with the VLA. The component light curves show $\sim 5\%$ variations in flux density from which we have measured the three independent time delays in this system: $\Delta t_{BA} = 31 \pm 7$ days, $\Delta t_{BC} = 36 \pm 7$ days, and $\Delta t_{BD} = 76^{+9}_{-10}$ days. These time delays are combined with the mass model of the lens presented in Paper II to give $H_0 = 59^{+8}_{-7}$ km s^{-1} Mpc^{-1} at 95% confidence (statistical) ± 15 km s^{-1} Mpc^{-1} (systematic). The statistical uncertainties represent the 95% confidence interval. The statistical uncertainties in the time delays can be reduced if a stronger variation in the background source is observed, while the systematic uncertainties may be reduced through the inclusion of the lensed extended emission in the lens modeling process. Our previous observations have shown that the background source in this system has varied by as much as 15% in the past, so we are conducting another program of monitoring. If a stronger variation is detected in the new data, the uncertainties on the time delays will be reduced and the accuracy of the measurement of H_0 with this system will be improved.

For generously donating portions of their VLA observing time to help us fill in gaps in our time coverage, we are grateful to Erik Leitch, Brian Mason, Jackie Hewitt, Cathy Trotter, Gillian Knapp, Michael Rupen, and James Gunn. The observations would not have been possible without the expertise and help provided by the VLA analysts and operators. We thank the anonymous referee for helpful comments. For useful discussions, we are indebted to Lori Lubin, Andy Biggs, Roger Blandford, Geoff Bower, Ketan Desai, Debbie Haarsma, Phillip Helbig, Jackie Hewitt, Tomislav Kundić, Erik Leitch, Chung-pei Ma, Mark Metzger, Chris Moore, Gerry Neugebauer, Frazer Owen, Michael Rupen, David Rusin, Martin Shepherd, and Ed Turner. This work is supported in part by the NSF under grant AST 94-20018 and by the European Commission, TMR Program, Research Network Contract ERBFMRXCT96-0034 "CERES."

REFERENCES

Bevington, P. R. 1969, Data Reduction and Error Analysis for the Physical Sciences (New York: McGraw-Hill)
Biggs, A. D., Browne, I. W. A., Helbig, P., Koopmans, L. V. E., Wilkinson, P. N., & Perley, R. A. 1999, MNRAS, 304, 349
Browne, I. W. A., Patnaik, A. R., Wilkinson, P. N., & Wrobel, J. M. 1998, MNRAS, 293, 257
Fassnacht, C. D., Womble D. S., Neugebauer, G., Browne, I. W. A., Readhead, A. C. S., Matthews, K., & Pearson, T. J. 1996, ApJ, 460, L103
Haarsma, D. B., Hewitt, J. N., Lehár, J., & Burke, B. F. 1999, ApJ, 510, 64
Högbom, J. 1974, ApJS, 15, 417
Jackson, N. J., Nair, S., & Browne, I. W. A. 1997, in Observational Cosmology with the New Radio Surveys, ed. M. Bremer, N. Jackson, & I. Perez-Fournon (Dordrecht: Kluwer), 315
Kochanek, C. S. 1995, ApJ, 445, 559
Koopmans, L. V. E., & Fassnacht, C. D. 1999, ApJ, 527, 513 (Paper II)
Kundić, T., et al. 1995, ApJ, 455, L5
———. 1997, ApJ, 482, 75
Lovell, J. E. J., Jauncey, D. L., Reynolds, J. E., Wieringa, M. H., King, E. A., Tzioumis, A. K., McCulloch, P. M., & Edwards, P. G. 1998, ApJ, 508, L51
Moore, C. B., & Hewitt, J. N. 1997, ApJ, 491, 451
Myers, S. T., et al. 1995, ApJ, 447, L5
Oscoz, A., Mediavilla, E., Goicoechea, L. J., Serra-Ricart, M., & Buitrago, J. 1997, ApJ, 479, L89
Patnaik, A. R., Browne, I. W. A., Wilkinson, P. N., & Wrobel, J. M. 1992, MNRAS, 254, 655
Pelt, J., Hjorth, J., Refsdal, S., Schild, R., & Stabell, R. 1998, A&A, 337, 681
Pelt, J., Hoff, W., Kayser, R., Refsdal, S., & Schramm, T. 1994, A&A, 286, 775
Pelt, J., Kayser, R., Refsdal, S., & Schramm, T. 1996, A&A, 305, 97

Perley, R. A., & Taylor, G. B. 1999, VLA Calibrator Manual (NRAO)
Refsdal, S. 1964, MNRAS, 128, 307
Schechter, P. L., et al. 1997, ApJ, 475, L85
Shepherd, M. C. 1997, in ASP Conf. Ser. 125, Astronomical Data Analysis Software and Systems VI, ed. G. Hunt & H. E. Payne (San Francisco: ASP), 77
Snellen, I. A. G., de Bruyn, A. G., Schilizzi, R. T., Miley, G. K., & Myers, S. T. 1995, ApJ, 447, L9
Walsh, D., Carswell, R. F., & Weymann, R. J. 1979, Nature, 279, 381
Weymann, R. J., et al. 1980, Nature, 285, 641
Wilkinson, P. N., Browne, I. W. A., Patnaik, A. R., Wrobel, J. M., & Soratia, B. 1998, MNRAS, 300, 790